Supplement of Atmos. Chem. Phys., 26, 3357–3390, 2026
https://doi.org/10.5194/acp-26-3357-2026-supplement

Atmospheric Chemistry and Physics
Open Access

Supplement of

Measurement report: Impact of domestic heating on dust deposition sources in hyper-arid Qaidam Basin, northern Qinghai-Xizang Plateau

Haixia Zhu et al.

Correspondence to: Suping Zhao (zhaosp@lzb.ac.cn) and Xiying Zhang (xyzhchina@isl.ac.cn)

Sect. S1

Collection efficiency of atmospheric dust deposition at monitoring sites

According to the study by Sow et al. (2006), for the MDCO, collection efficiency is higher at low wind speeds but decreases rapidly as wind speed increases. Additionally, efficiency declines significantly with increasing particle size of atmospheric dust deposition. In this study, the sampling efficiency was calculated using Eq (1):

$$E=p[\cos(2H)+q\cos(4H)]+r \quad \text{(Eq. S1)}$$

where: E = efficiency; H = MDCO orientation (in radians). H=0 when the MDCO is parallel to the airflow, and H=π/2 when perpendicular. This formula accurately computes efficiency values measured in wind tunnel experiments.

The coefficients p, q, and r are determined based on local dust particle size and wind speed. Since the mean size of dust particle at all monitoring sites in this study ranged from 20 to 40 μm, coefficients were uniformly calculated using Eqs. (2-4):

$$p=-0.0001487u^6+0.0039875u^5-0.0430022u^4+0.2363859u^3-0.6819261u^2+0.8975262u-0.19002 \quad \text{(Eq. S2)}$$

$$q=0.0011874u^6-0.0267361u^5+0.2292733u^4-0.9326238u^3+1.827994u^2-1.5175786u+0.5077858 \quad \text{(Eq. S3)}$$

$$r=0.0000704u^6-0.0011765u^5+0.004459u^4+0.0178979u^3-0.113394u^2-0.0988192u+0.9562646 \quad \text{(Eq. S4)}$$

Based on the wind speed and particle size conditions at each monitoring site, the calculated sampling efficiencies are presented in the table below.

Wind speed and sampling efficiency at atmospheric dust deposition monitoring stations

Sites	Wind speed($m \cdot s^{-1}$)	Efficiency (%)
Xiao Zaohuo (XZH)	3.34	9.98
Golmud (GEM)	1.91	34.85
Da Gele (LTC)	3.73	7.09
Nuo Muhong (NMH)	1.46	44.55
Balong (BLX)	3.38	9.46
Dulan (DLX)	2.35	25.82

Sect. S2.

PMF Source apportionment initialization

The source apportionment of dust deposition utilized the EPA PMF 5.0 model to analyze 109 samples based on their respective sampling sites. Internal PMF parameters, such as Q_{robust}, Q_{true}, and $Q_{expected}$ were considered to assess performance of PMF. In general, Q is a measure of the fitness of the model; Q_{robust} is calculated using only samples that fit the model well, while all samples are used in calculating Q_{true}. $Q_{expected}$ is equal to the number of samples multiplied by the number of strong species. Multiple iterations of each dataset were processed to identify consistent Q values. Testing for factor peak values across 3 to 6 factors revealed that 4 factors provided the best solution for XZH, LTC, and BLX, while 5 factors were optimal for GEM, NMH, and DLX (Figure S14). High determination coefficients (R^2 = 0.64~0.98) indicated a strong correlation between calculated and measured element fluxes, with intercepts and slopes nearing unity. The extra modeling uncertainty is 0%. The analysis found no need for factor rotation, and the Q_{robust} values closely aligned with the Q_{true}, suggesting a good model fit. Bootstrapping was not used because of the small size of the sample set. High uncertainties were observed in the contribution of certain species to each factor, but each factor contained at least one well-constrained species, highlighting the dominant chemical characteristic of that factor. These high uncertainties stem, in part, from the high and variable values of field blanks that are carried through the model. Rotational swaps, indicating uncertainty in the identified components and their contributions, were not observed during displacement, and the largest change in Q was -0.01%, evidencing the good fit of the solution set.

A theoretical Q-value (also referred to Q_{exp}) may be approximated as a number of points in the data matrix minus the total number of elements in the factor matrices (Paatero and Tapper, 1994)

$$Q_{exp} = n \cdot m - N \cdot (n + m), \quad \text{(Eq. S5)}$$

where n is the number of samples, m is the number of species and N is the number of obtained factors. Large deviation from the Q_{exp} may indicate that a larger extra modeling uncertainty is needed. The optimal number of factors was determined based on the variation in the Q_{robust}/Q_{exp} ratio and the interpretability of the analytical factor distribution. In our study, the Q_{true}/Q_{robust} ratios for the PMF models at all six monitoring stations were below 1.5, indicating that the simulation results are reasonable. Additionally, the Q_{robust}/Q_{exp} ratio confirms that our simulated results align

with the optimal number of factors.

Error estimates of the base PMF solution are provided through combination of Displacement (DISP) and Bootstrap (BS) tests (DISP-BS). Displacement test explores the rotational ambiguity of the solution by assessing the largest range of source profiles without significant increase in the Q value. DISP%dQ is the parameter displaying in the displacement result matrix. If DISP%dQ is equal to zero that means the displacement analysis result is considered as acceptable. The displacement swap counts (DISP swaps) are a key indicator of the stability of a PMF solution. If it swaps it indicates that there is significant rotational ambiguity and that the solution is not sufficiently robust to be used. Error estimates of the base solution are provided through combination of both Displacement (DISP), and Bootstrap (BS) tests (DISP-BS) (Manousakas et al., 2017).

BS detects disproportionate effects of a small set of observations on the solution and also, to a lesser extent, effects of rotational ambiguity. Mapping of bootstrap factors to base factors is a summary result on factors mapping. Ideally BS factor mapping should be one-to-one with respect to base run factors. Nevertheless, factors with more than 80% mapping are considered acceptable. Base random seed is the seed number corresponding to the result with minimum Q and allows reproducing the same results of PMF solution.

In our study, the decline in DISP%dQ remained consistently within 0.1%, indicating that the global minima of dQ were achieved under the tested configurations. Throughout the four dQmax levels, no factor switching occurred during the DISP run phase, and the factor matching rate during the BS phase exceeded 85%. Additionally, there was no factor switching in the BS-DISP run phase. These findings underscore the stability of the PMF model results (Paatero et al., 2014; Brown et al., 2015; Li, 2020).

Reference

Brown, S.G., Eberly, S., Paatero, P. and Norris, G.A. (2015) Methods for estimating uncertainty in PMF solutions: examples with ambient air and water quality data and guidance on reporting PMF results. Science of the Total Environment 518-519, 626-635.

Li, J., Teng, Wu, J., Chen, H., and Jiang, J. (2020) Uncertainty in identifying soil heavy metal sources using the PMF model (in Chinese). China Environmental Science 40(2), 716-725.

Manousakas, M., Papaefthymiou, H., Diapouli, E., Migliori, A., Karydas, A., Bogdanovic-Radovic, I. and Eleftheriadis, K. (2017) Assessment of PM2. 5 sources and their corresponding level of uncertainty in a coastal urban area using EPA PMF 5.0 enhanced diagnostics. Science of the Total Environment 574, 155-164.

Paatero, P., Eberly, S., Brown, S.G. and Norris, G.A. (2014) Methods for estimating uncertainty in factor analytic solutions. Atmospheric Measurement Techniques 7(3), 781-797.

Paatero, P. and Tapper, U. (1994) Positive matrix factorization: A non-negative factor model with optimal utilization of error estimates of data values. Environmetrics 5(2), 111-126.

Sow, M., Goossens, D., and Rajot, J. L.(2006) Calibration of the MDCO dust collector and of four versions of the inverted frisbee dust deposition sampler. Geomorphology, 82, 360-375.

Supplement Tables

Stations	Latitude (°)	Longitude (°)	Description	Height (m)	Surrounding environment
XZH	93.68	36.80	*Lycium* berry cultivation base, national climate benchmark station	15	Sampler installed on the rooftop of a 3-story building at Xiaozhuohuo Meteorological Station. The area is open, with no other structures within 1 km; entirely agricultural land
GEM	94.91	36.42	The largest city in the Qaidam Basin, with a high population	10	Sampler placed on the rooftop of a 2-story building at Golmud Meteorological Bureau. Surroundings include public facilities; a road is 50 m away. Urban heating is primarily central or natural gas-based
LTC	95.77	36.49	Desert with camel breeding farms	3	Sampler located on the rooftop of a single-story building at Dageliao Camel Farm. The area is sparsely populated and largely undisturbed
NMH	96.43	36.44	Towns with extensive *Lycium* berry cultivation in the surrounding areas	1.5	Sampler installed at Nuomuhong Meteorological Station (~1.5 m above ground). Adjacent to a road. Local heating relies on household coal and biomass fuels
BLX	97.54	36.16	Pasture with developed agricultural practices	3	Sampler mounted on the rooftop of a single-story dwelling of a Tibetan herder in Balong Township. Sparse residential presence; distant from major roads
DLX	98.10	36.30	County seat with a relatively large population and a thriving mining industry	20	Sampler positioned on the rooftop of a 4-story building at Dulan Meteorological Bureau. Nearby roads present. Heating primarily from household coal and biomass fuels

Table S1 Geographic coordinates and descriptions of monitoring stations in the study area. The table lists the latitude and longitude of each site, along with a brief description of the local characteristics and land use. [XZH, Xiao Zaohuo station; GEM, Golmud station; LTC, Da Gele station; NMH, Nuo Muhong station; BLX, Balong station; DLX, Dulan station].

	Rural-HP	Rural-NHP	Urban-HP	Urban-NHP
Q_{exp}	225	165	340	332
Q_{robust}	1272.23	809.67	1024.57	1921.00
Q_{true}	1614.83	1006.44	1364.86	2591.24
Q_{true}/Q_{robust}	1.27	1.24	1.33	1.35
Q_{robust}/Q_{exp}	7.18	6.10	4.01	7.80
Converged	Yes	Yes	Yes	Yes
DISP % *dQ*	<0.1%	<0.1%	<0.1%	<0.1%
DISP % swaps	0%	0%	0%	0%
BS R^2	0.6	0.6	0.6	0.6
BS mapping	91%	94%	89%	80%
BS-DISP %swaps	0%	0%	0%	0%

Table S2 Summary of PMF and error estimate diagnostics. HP, domestic heating period; NHP, non-domestic heating period.

	Base Value	BS 5th	BS 50th	BS 95th	DISP Min	DISP Average	DISP Max	BS-DISP 5th	BS-DISP average	BS-DISP 95th
Salt lake	0.2	0.1	0.3	2.7	0.1	0.3	0.5	0.0	1.4	2.8
Biomass burning	1.2	1.1	1.5	4.1	1.2	1.4	1.6	0.0	0.2	2.3
Industry	0.7	0.2	0.5	1.1	0.3	0.6	0.8	0.0	0.8	1.7
Coal combustion	1.1	0.5	0.8	2.4	1.2	1.3	1.6	0.0	0.8	1.7
Soil dust	1.8	0.8	1.7	2.9	1.5	1.9	2.2	0.0	2.3	4.7
Traffic emission	1.8	1.0	1.6	3.3	1.7	1.8	1.9	0.0	1.6	5.2
Secondary formation	0.1	0.1	1.1	2.3	0.3	0.6	0.8	0.0	0.8	1.7

Table S3 Uncertainty tools' results for dust deposition flux (mg/g).

Site	Souces	TC	OC	EC	OC/EC	Char-EC	Soot-EC	Char/soot	Reference
Gwangju (Korea)	Road dust	31.97	27.15	4.82	5.63	/	/	/	(Lee et al., 2018)
Ulaanbaatar (Mongolia)	Road dust	8.43	7.17	1.26	5.69	/	/	/	(Lee et al., 2018)
Bolu (Turkey)	Road dust	605.2	533	72.2	7.38	53.7	18.5	2.90	(Demir et al., 2022)
E'zhou (Hubei)	Road dust	18.29	5.35	12.84	0.42	/	/	/	(Zhang et al., 2016)
Kumasi (West African)	Road dust	28.00	26.45	1.55	17.07	1.19	0.36	3.31	(Bandowe et al., 2019)
Xian	Road dust	36.53	31.01	5.52	5.62	2.75	2.77	0.99	(Wei et al., 2015)
Huainan	Road dust	27.11	25.9	1.21	21.40	0.59	0.27	2.19	(Liu et al., 2020)
Guwahati (India)	Road dust	21.50	0.80	20.70	0.16	/	/	/	(Hussain et al., 2015)
Wuhan	Road dust	3.50	1.29	2.21	0.85	0.17	2.04	0.09	(Liu et al., 2021)
New Delhi (India)	Dust-fall	61.63	56.5	5.13	11.01	/	/	/	(Mishra and Kulshrestha, 2017)
Xian	Dust-fall	14.6	7.4	7.2	1.03	/	/	/	（Han et al., 2009）
Huangshi	Dust-fall	36.61	25.15	11.46	2.19	/	/	/	（Zhan et al., 2016）
Nanchang	Dust-fall	24.46	15.18	9.28	1.64	/	/	/	(Zhang, 2014)
Beijing	Dust-fall	47.2	41.5	5.7	8.9	/	/	/	(Tang et al., 2013)
Tianjin	Road dust	13.17	10.63	2.54	4.05	/	/	/	(Ma et al., 2019)
Shijiazhuang	Road dust	20.65	18.34	2.29	5.83	/	/	/	(Guo et al., 2018)
Wuhu	Dust-fall	33.26	22.49	10.77	2.09	/	/	/	(Deng et al., 2014)
Xiaogan	Dust-fall	5.77	4.32	1.45	2.98	/	/	/	(Zhan et al., 2022)
Qaidam Basin	Dust-fall	4.87	3.48	1.41	7.09	1.14	0.25	4.97	This study

Table S4 Comparison of carbonaceous element concentrations in dust-fall from this study with those from other global regions.

City	Country	Element					Reference
		Cd	Cr	Cu	Pb	Zn	
Guangzhou	China	4.22±1.21	62.2±27.1	116±30	72.6±17.9	504±191	Cai et al., 2013
Xi'an	China	4.18±1.20	195.92±48.66	125.31±78.80	310.29±80.79	721.20±237.57	Chen et al., 2017
Suzhou	China	2.45±4.89	25.7±15.4	104.8±214.9	262.2±494.4	376.9±712.4	Ma et al., 2016
Changsha	China	9.11	80.7	43.9	66.6	215	Li et al., 2016
Beijing	China	0.72±0.74	84.7±30.8	69.9±68.3	105±223	222±120	Wei et al., 2015
Tianjin	China	0.45	71.85	55.47	254	–	Yu et al., 2014
Huainan	China	0.25	61.1	36.3	42.6	–	Tang et al., 2017
Shanghai	China	1.23	159.3	196.8	294.9	733.8	Shi et al., 2008
Lanzhou	China	0.81±0.72	96.9±54.6	77.4±19.8	34.7±12.2	56.6±40.6	Jiang et al., 2018
Jinan	China	0.24	135.95	–	110.78	380.22	Pang et al., 2014
Galicia	Spain	0.31±0.13	54.1±10.8	20.5±11.3	11.7±33.1	98.7±71.3	Franco-Uria et al., 2009
Alexandria	Egypt	0.33	24.3	79.7	70.3	169	Dat et al., 2021
Ho Chi Minh City,	Vietnam	0.5	102.4	153.7	49.6	466.4	Jadoon et al., 2021
Cantabria region	Spain	0.1	5.2	11.8	4.5	183	Fernandez-Olmo et al., 2015
Junggar Basin	China	16.65	605.5	100.1	–	5933.9	(Yang et al., 2016)
Ebinur Basin	China	0.34±0.037	102.17±3.57	24.52±3.11	16.32±1.02	157.16±5.14	(Abuduwailil et al., 2015)
Qaidam Basin	China	0.47±0.45	7.38±6.90	8.12±6.82	14.82±14.23	58.47±52.05	This study

Table S5 Comparison of dust-fall metal concentrations in this study with those from other regions.

	Rural-HP		Rural-NHP		Urban-HP		Urban-NHP	
	Contribution	Error	Contribution	Error	Contribution	Error	Contribution	Error
Industry	13.95	0.26	13.20	0.33	6.69	0.18	25.55	0.66
Salt lake	4.97	0.55	19.61	0.53	11.58	0.61	2.16	1.12
Soil dust	9.04	0.44	33.23	0.43	19.11	0.10	6.84	0.93
Coal combustion	30.38	0.18	N/A	N/A	23.31	0.24	N/A	N/A
Traffic emission	N/A	N/A	8.52	0.50	32.91	0.39	60.75	0.28
Biomass burning	41.67	0.22	25.43	0.78	6.41	0.27	N/A	N/A
Secondary inorganics	N/A	N/A	N/A	N/A	N/A	N/A	4.70	1.04

Table S6 Sources contribution and corresponding error. HP, heating period; NHP, non-heating period.

Reference

Bandowe, B. A. M., Nkansah, M. A., Leimer, S., Fischer, D., Lammel, G., and Han, Y.: Chemical (C, N, S, black carbon, soot and char) and stable carbon isotope composition of street dusts from a major West African metropolis: Implications for source apportionment and exposure, Science of The Total Environment, 655, 1468-1478, https://doi.org/10.1016/j.scitotenv.2018.11.089, 2019.

Brown, S.G., Eberly, S., Paatero, P., Norris, G.A. (2015) Methods for estimating uncertainty in PMF solutions: examples with ambient air and water quality data and guidance on reporting PMF results. Sci Total Environ 518-519, 626-635.

Cai, Q.Y., Mo, C.H., Li, H.Q., Lu, H., Zeng, Q.Y., Li, Y.W., Wu, X.L. (2013) Heavy metal contamination of urban soils and dusts in Guangzhou, South China. Environ Monit Assess 185, 1095-1106.

Chen, Y., Zhao, J. J, Tang, D., Tian, X. L and Wu, Y.G. (2017) Characteristics of heavy metal pollution and ecological risk of atmospheric dust-fall in Xi'an (in Chinese). Arid Zone Resources and Environment 31, 154-159.

Dat, N.D., Nguyen, V.T., Vo, T.D., Bui, X.T., Bui, M.H., Nguyen, L.S.P., Nguyen, X.C., Tran, A.T., Nguyen, T.T., Ju, Y.R., Huynh, T.M., Nguyen, D.H., Bui, H.N., Lin, C. (2021) Contamination, source attribution, and potential health risks of heavy metals in street dust of a metropolitan area in Southern Vietnam. Environ Sci Pollut Res Int 28, 50405-50419.

Demir, T., Karakaş, D., and Yenisoy-Karakaş, S.: Source identification of exhaust and non-exhaust traffic emissions through the elemental carbon fractions and Positive Matrix Factorization method, Environmental Research, 204, 112399, https://doi.org/10.1016/j.envres.2021.112399, 2022.

Deng, Z., Fang, F., Jiang, P., Zhang, J., and Lin, Y.: Distribution characteristics of black carbon in surface dust from the urban area of Wuhu City, Journal of Anhui Normal University (Natural Science Edition), 37, 58-62, https://doi.org/10.14182/j.cnki.1001-2443.2014.01.009, 2014.

Fernandez-Olmo, I., Puente, M., Irabien, A. (2015) A comparative study between the fluxes of trace elements in bulk atmospheric deposition at industrial, urban, traffic, and rural sites. Environ Sci Pollut Res Int 22, 13427-13441.

Franco-Uria, A., Lopez-Mateo, C., Roca, E., Fernandez-Marcos, M.L. (2009) Source identification of heavy metals in pastureland by multivariate analysis in NW Spain. J Hazard Mater 165, 1008-1015.

Jadoon, W.A., Abdel-Dayem, S., Saqib, Z., Takeda, K., Sakugawa, H., Hussain, M., Shah, G.M., Rehman,

W., Syed, J.H. (2021) Heavy metals in urban dusts from Alexandria and Kafr El-Sheikh, Egypt: implications for human health. Environ Sci Pollut Res Int 28, 2007-2018.

Jiang, Y., Shi, L., Guang, A.L., Mu, Z., Zhan, H., Wu, Y. (2018) Contamination levels and human health risk assessment of toxic heavy metals in street dust in an industrial city in Northwest China. Environ Geochem Health 40, 2007-2020.

Hussain, K., Rahman, M., Prakash, A., and Hoque, R. R.: Street dust bound PAHs, carbon and heavy metals in Guwahati city – Seasonality, toxicity and sources, Sustainable Cities and Society, 19, 17-25, https://doi.org/10.1016/j.scs.2015.07.010, 2015.

Guo, S., Wang, L., Zhou, P., Guo, S., Qin, W., An, S., Xiao, J., Liu, J., and Ji, Y.: Characteristics and sources of organic carbon and elemental carbon in road dust during summer in Shijiazhuang, Environmental Engineering, 36, 122-126, https://doi.org/10.13205/j.hjgc.201804025, 2018.

Lee, K. Y., Batmunkh, T., Joo, H. S., and Park, K.: Comparison of the physical and chemical characteristics of fine road dust at different urban sites, Journal of the Air & Waste Management Association, 68, 812-823, 10.1080/10962247.2018.1443855, 2018.

Li, F., Zhang, J., Huang, J., Huang, D., Yang, J., Song, Y., Zeng, G. (2016) Heavy metals in road dust from Xiandao District, Changsha City, China: characteristics, health risk assessment, and integrated source identification. Environ Sci Pollut Res Int 23, 13100-13113.

Li, J., Teng, W. J., Chen, H. Y and Jiang, J. Y. (2020) Uncertainty in identifying sources of soil heavy metals using the PMF model (in Chinese). China Environmental Science 40, 716-725.

Liu, Y., Liu, G., Yousaf, B., Zhang, J., and Zhou, L.: Carbon fractionation and stable carbon isotopic fingerprint of road dusts near coal power plant with emphases on coal-related source apportionment, Ecotoxicology and Environmental Safety, 202, 110888, https://doi.org/10.1016/j.ecoenv.2020.110888, 2020.

Liu, Z., Cheng, J., Li, C., Gao, Y., Zhan, C., Liu, S., Zhang, J., and Liu, H.-X.: Pollution characteristics and source analysis of carbon components in road dust from Qingshan District, Wuhan City, Environmental Chemistry, 40, 772-778, 2021.

Ma, Y., Ji, Y., Guo, J., Zhao, J., Li, Y., Wang, S.-B., and Zhang, L.: Characteristics and source analysis of carbon components in road dust estimated by the quadrat method during spring in Tianjin, Acta Scientiae Circumstantiant, 40, 2540-2545, https://doi.org/10.13227/j.hjkx.201811259, 2019.

Ma, Z., Chen, K., Li, Z., Bi, J., Huang, L. (2015) Heavy metals in soils and road dusts in the mining areas of Western Suzhou, China: a preliminary identification of contaminated sites. Journal of Soils and Sediments 16, 204-214.

Mishra, M. and Kulshrestha, U.: Chemical characteristics and deposition fluxes of dust-carbon mixed coarse aerosols at three sites of Delhi, NCR, Journal of Atmospheric Chemistry, 74, 399-421, 10.1007/s10874-016-9349-1, 2017.

Paatero, P., Eberly, S., Brown, S.G., Norris, G.A. (2014) Methods for estimating uncertainty in factor analytic solutions. Atmospheric Measurement Techniques 7, 781-797.

Paatero, P., Tapper, U. (1994) Positive matrix factorization: A non-negative factor model with optimal utilization of error estimates of data values. Environmetrics 5, 111-126.

Pang, X. G., Wang, X. M., Dai, J. R., Guo, R. P., Yu, C., Cui, Y. J and Dong, J. (2014) Geochemical characteristics and pollutant end-member study of atmospheric dust-fall in Jinan (in Chinese). Chinese Geology 41, 285-293.

Shi, G., Chen, Z., Xu, S., Zhang, J., Wang, L., Bi, C., Teng, J. (2008) Potentially toxic metal contamination of urban soils and roadside dust in Shanghai, China. Environ Pollut 156, 251-260.

Tang, Y., Han, G., and Xu, Z.: Characteristics of black carbon content in atmospheric dust fall in Beijing and its northern areas, Acta Scientiae Circumstantiant, 33, 332-338, https://doi.org/10.13671/j.hjkxxb.2013.02.033, 2013.

Tang, Z., Chai, M., Cheng, J., Jin, J., Yang, Y., Nie, Z., Huang, Q., Li, Y. (2017) Contamination and health risks of heavy metals in street dust from a coal-mining city in eastern China. Ecotoxicol Environ Saf 138, 83-91.

Wei, C., Bandowe, B. A. M., Han, Y., Cao, J., Zhan, C., and Wilcke, W.: Polycyclic aromatic hydrocarbons (PAHs) and their derivatives (alkyl-PAHs, oxygenated-PAHs, nitrated-PAHs and azaarenes) in urban road dusts from Xi'an, Central China, Chemosphere, 134, 512-520, https://doi.org/10.1016/j.chemosphere.2014.11.052, 2015.

Wei, X., Gao, B., Wang, P., Zhou, H., Lu, J. (2015) Pollution characteristics and health risk assessment of heavy metals in street dusts from different functional areas in Beijing, China. Ecotoxicol Environ Saf 112, 186-192.

Yang, C., Tashpolat, T., Hou, Y.-J., Gao, Y.-X., Liu, F., Xia, N. (2016) [Assessment of Heavy Metals Pollution and Its Health Risk of Atmospheric Dust Fall from East Part of Junggar Basin in

Xinjiang]. Huan jing ke xue= Huanjing kexue 37, 2453-2461.

Yu, B., Wang, Y., Zhou, Q. (2014) Human health risk assessment based on toxicity characteristic leaching procedure and simple bioaccessibility extraction test of toxic metals in urban street dust of Tianjin, China. PLoS One 9, e92459.

Zhan, C., Zhan, J., Ke, Z., Liu, S., Zhang, J., and Liu, H.: Pollution characteristics and source analysis of black carbon in different types of dust in Xiaogan City, Hubei Province, Environmental Pollution & Control, 44, 14-19+26, https://doi.org/10.15985/j.cnki.1001-3865.2022.01.003, 2022.

Zhang, F.: Study on dry deposition of organic carbon and elemental carbon in the atmosphere of Nanchang City, [Master's thesis], 2014.

Zhang, J., Zhan, C., Liu, H., Liu, T., Yao, R., Hu, T., Xiao, W., Xing, X., Xu, H., and Cao, J.: Characterization of Polycyclic Aromatic Hydrocarbons (PAHs), Iron and black carbon within street dust from a steel industrial city, Central China, Aerosol and Air Quality Research, 16, 2452-2461, 10.4209/aaqr.2016.02.0085, 2016.

Supplement Figures

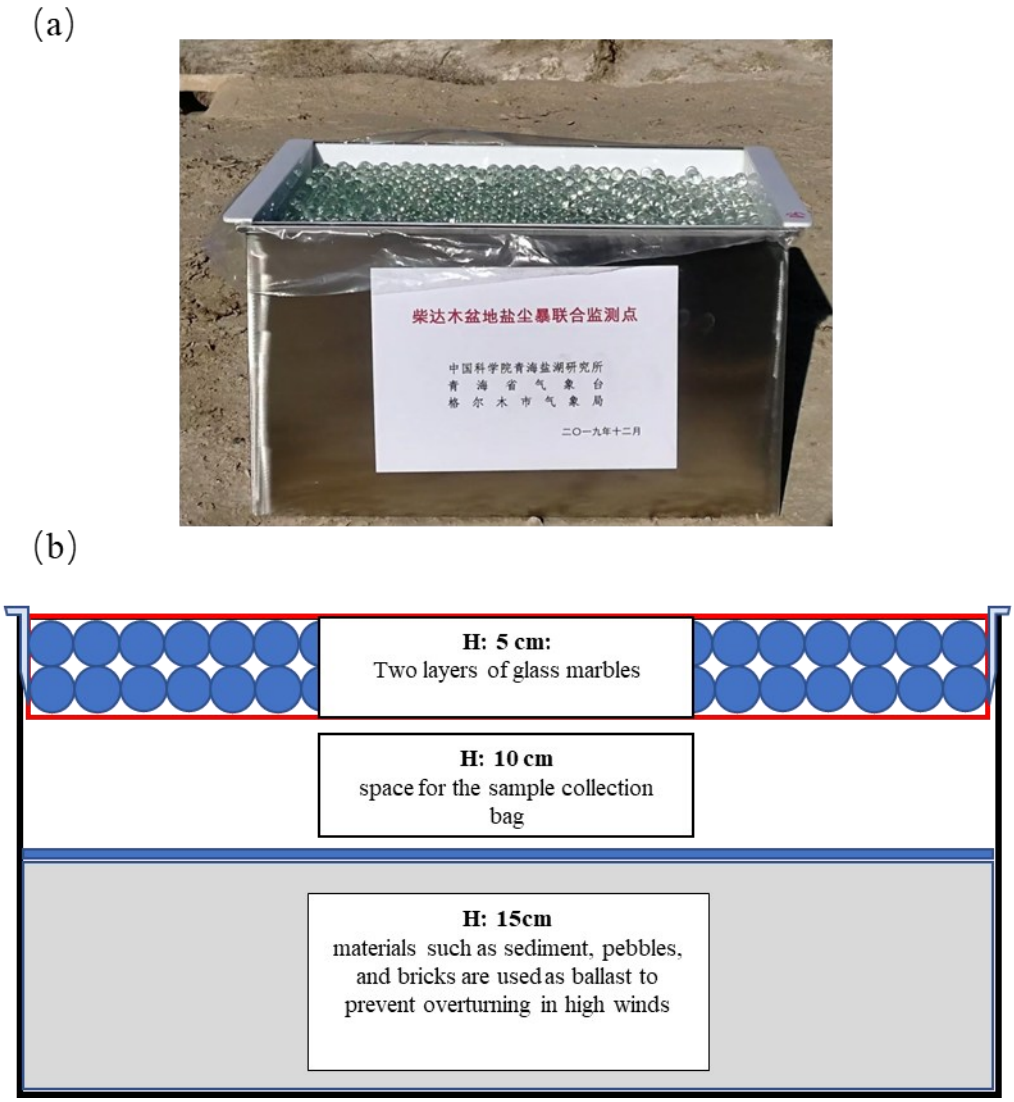

Figure S1. (a) Photo and (b) schematic of dust samples sampling device. The device is a stainless steel box measuring 50 cm in length, 30 cm in width, and 30 cm in height, consisting of three layers. The first layer, 5 cm deep, contains two layers of φ16 mm glass beads with a specific density. The second layer, 10 cm high, contains high-density polyethylene bags for dust collection. The third layer, 15 cm high, is constructed from sand pebble brick material to ensure equipment stability.

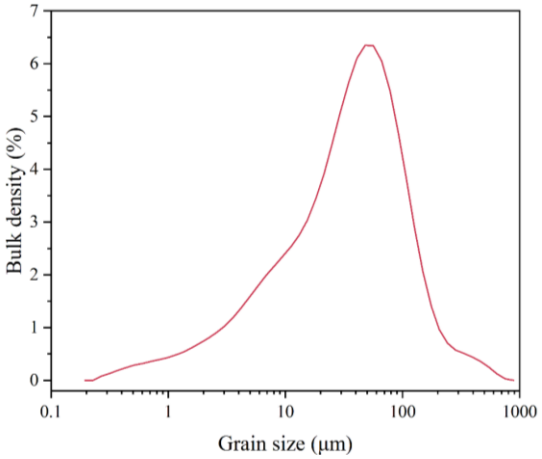

Figure S2 Particle size distribution characteristics of atmospheric dust-fall. This figure presents the results obtained from the particle size analysis of dust-fall samples collected in this study.

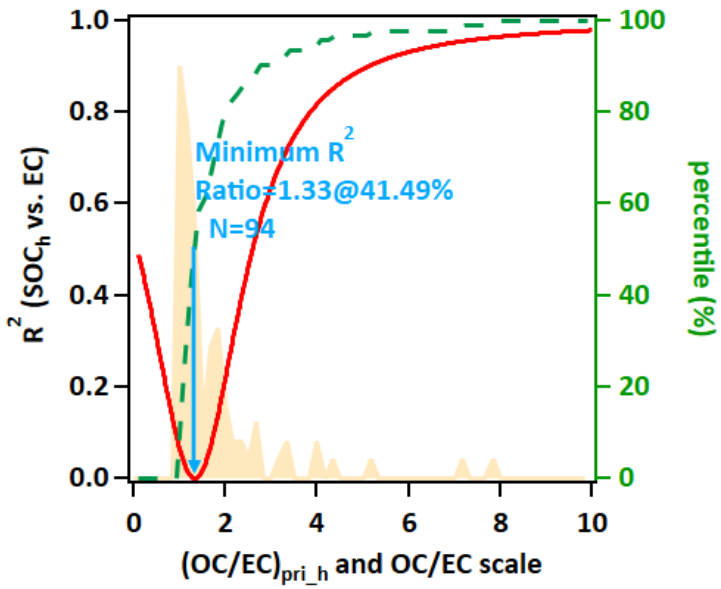

Figure S3 (OC/EC) ratio when minimum R^2 is observed between SOC and EC measurement data. The $(OC/EC)_{pri\_h}$ is defined as the hypothetical primary OC/EC ratio. The red line plots the R^2 between the tracer species (EC) for each value of $(OC/EC)_{pri\_h}$ (X-axis) and the estimated secondary organic carbon (SOC_h). The shaded area is the frequency distribution of the OC/EC ratio, and green percentile represents the cumulative frequency rate. N represents the number of the total measurement data set.

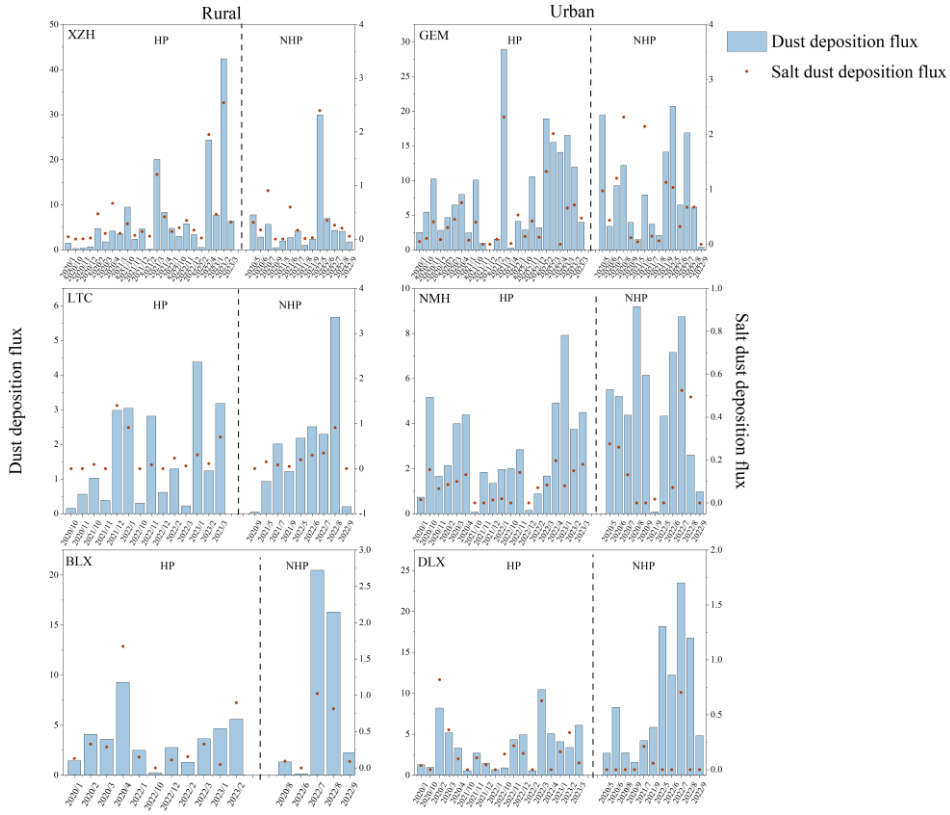

Figure S4 Temporal variation of atmospheric dust (DF) and salt dust deposition flux (SDF) at six stations during heating and non-heating periods. DF represented by blue bars and SDF by red circles. [HP, Heating period; NHP, Non-heating period; XZH, Xiao Zaohuo station; GEM, Golmud station; LTC, Da Gele station; NMH, Nuo Muhong station; BLX, Balong station; DLX, Dulan station].

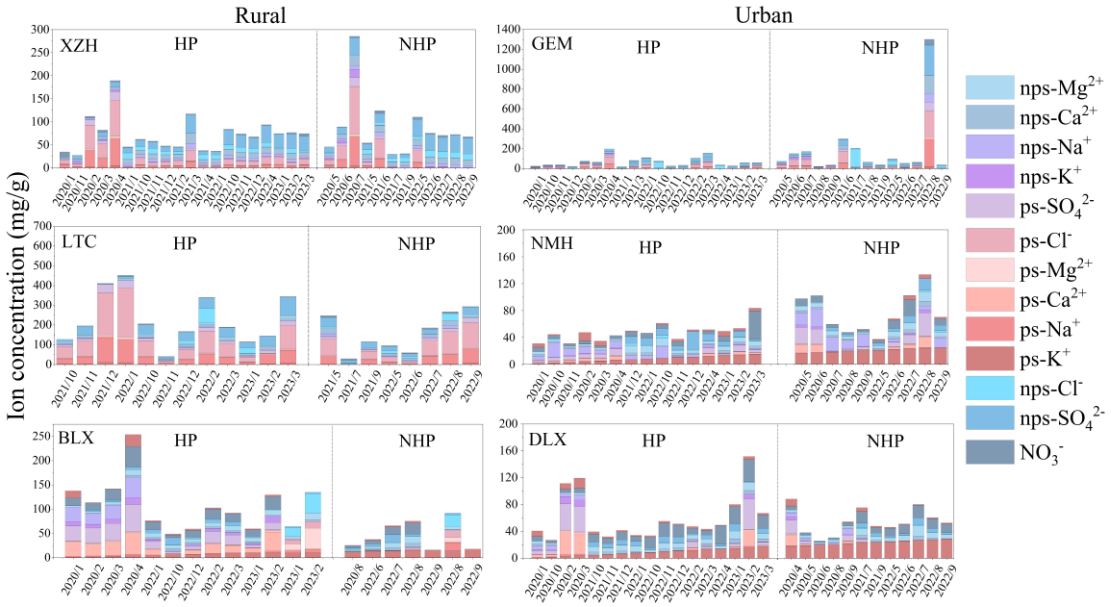

Figure S5 Temporal variations in ion concentrations at six monitoring sites during heating and non-heating periods. HP, Heating period; NHP, Non-heating period; XZH, Xiao Zaohuo station; GEM, Golmud station; LTC, Da Gele station; NMH, Nuo Muhong station; BLX, Balong station; DLX, Dulan station.

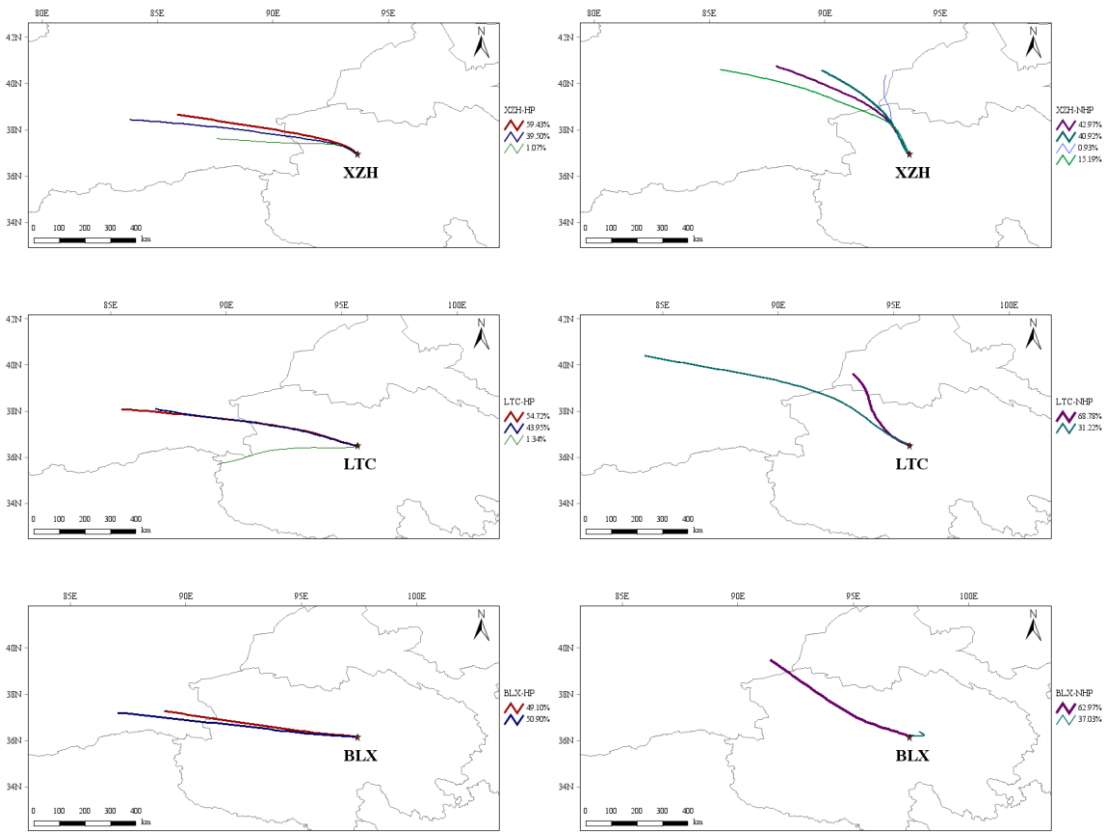

Figure S6 Backward trajectory simulations were conducted at rural monitoring stations during heating and non-heating periods. Different colors denote distinct trajectory paths, while line thickness indicates the degree of contribution from each path. The red star marks the location of the stations. [HP, Heating period; NHP, Non-heating period; XZH, Xiao Zaohuo station; LTC, Da Gele station; BLX, Balong station].

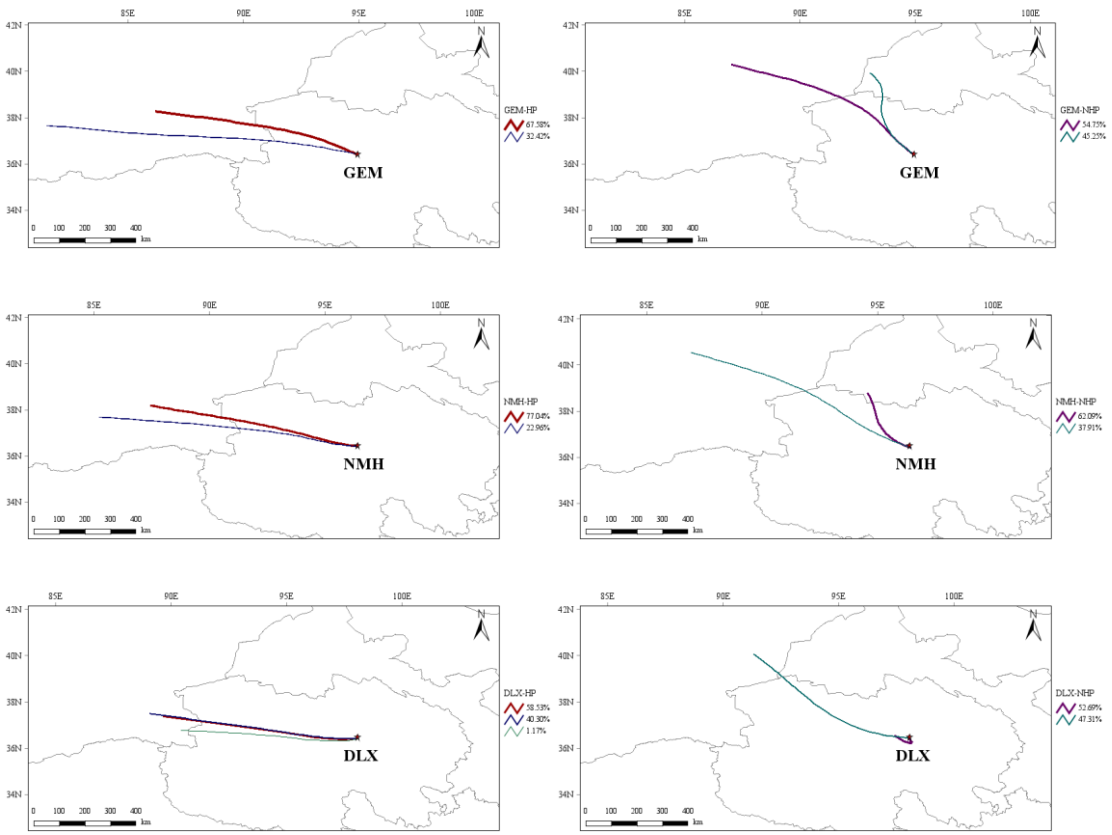

Figure S7 Backward trajectory simulations were conducted at urban monitoring stations during heating and non-heating periods. Different colors denote distinct trajectory paths, while line thickness indicates the degree of contribution from each path. The red star marks the location of the stations. [HP, Heating period; NHP, Non-heating period; GEM, Golmud station; NMH, Nuo Muhong station; DLX, Dulan station].

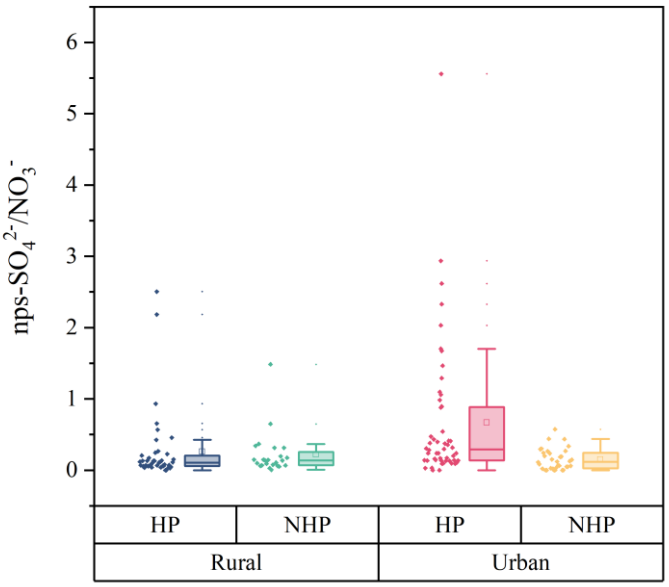

Figure S8 The ratio of nps-SO_4^{2-} to NO_3^- in soluble ions during heating and non-heating periods in rural and urban areas. HP: heating period; NHP: non-heating period.

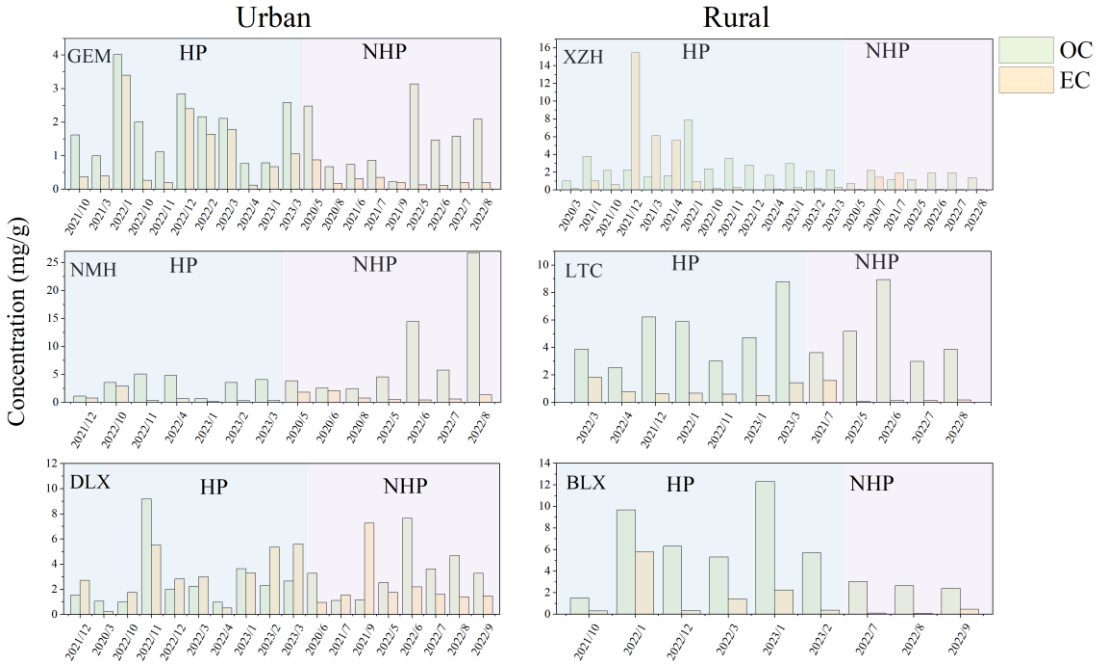

Figure S9 Temporal variations in organic (OC) and element carbon (EC) concentration at six monitoring sites during heating and non-heating periods. HP, Heating period; NHP, Non-heating period; XZH, Xiao Zaohuo station; GEM, Golmud station; LTC, Da Gele station; NMH, Nuo Muhong station; BLX, Balong station; DLX, Dulan station.

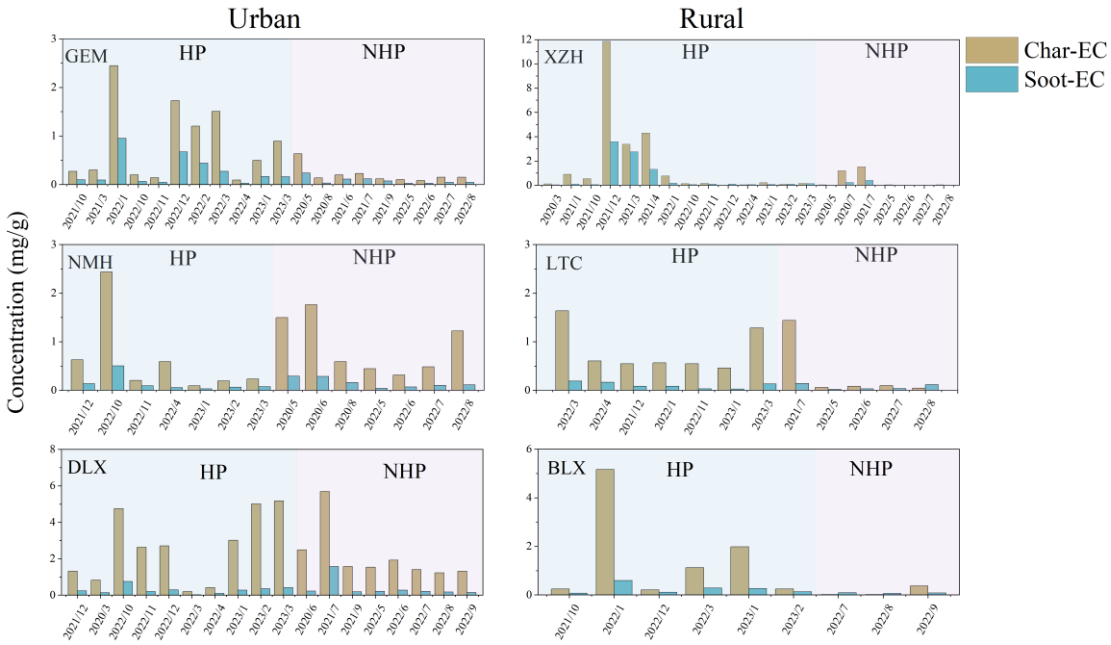

Figure S10 Temporal variations in Char-OC and Soot-EC concentration at six monitoring sites during heating and non-heating periods. HP, Heating period; NHP, Non-heating period; XZH, Xiao Zaohuo station; GEM, Golmud station; LTC, Da Gele station; NMH, Nuo Muhong station; BLX, Balong station; DLX, Dulan station.

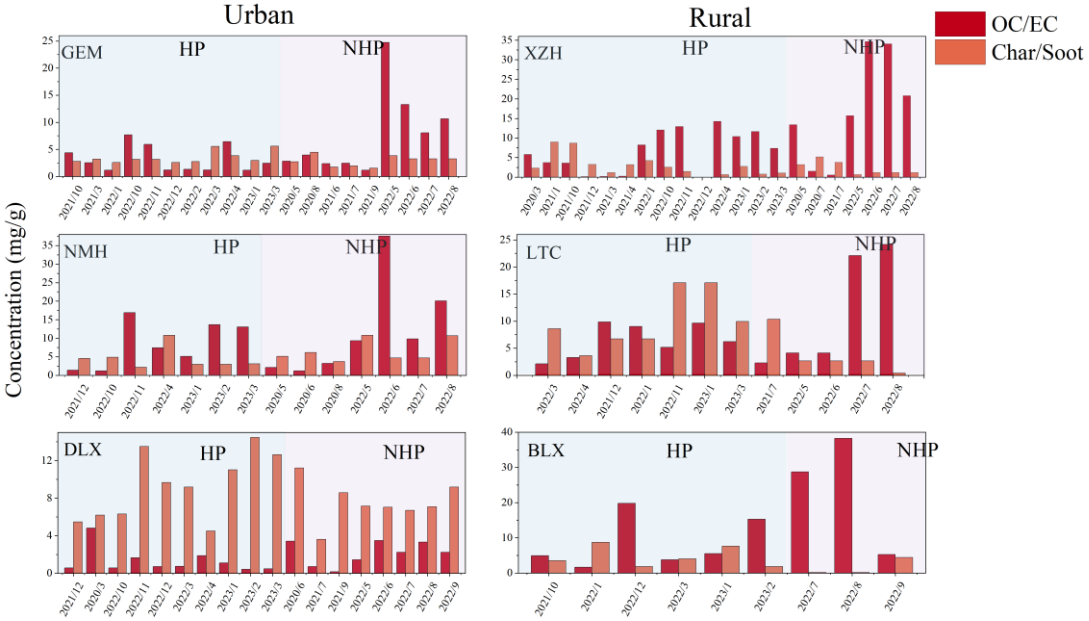

Figure S11 Temporal variations in OC/EC and Char/Soot ratio at six monitoring sites during heating and non-heating periods. HP, Heating period; NHP, Non-heating period; XZH, Xiao Zaohuo station; GEM, Golmud station; LTC, Da Gele station; NMH, Nuo Muhong station; BLX, Balong station; DLX, Dulan station.

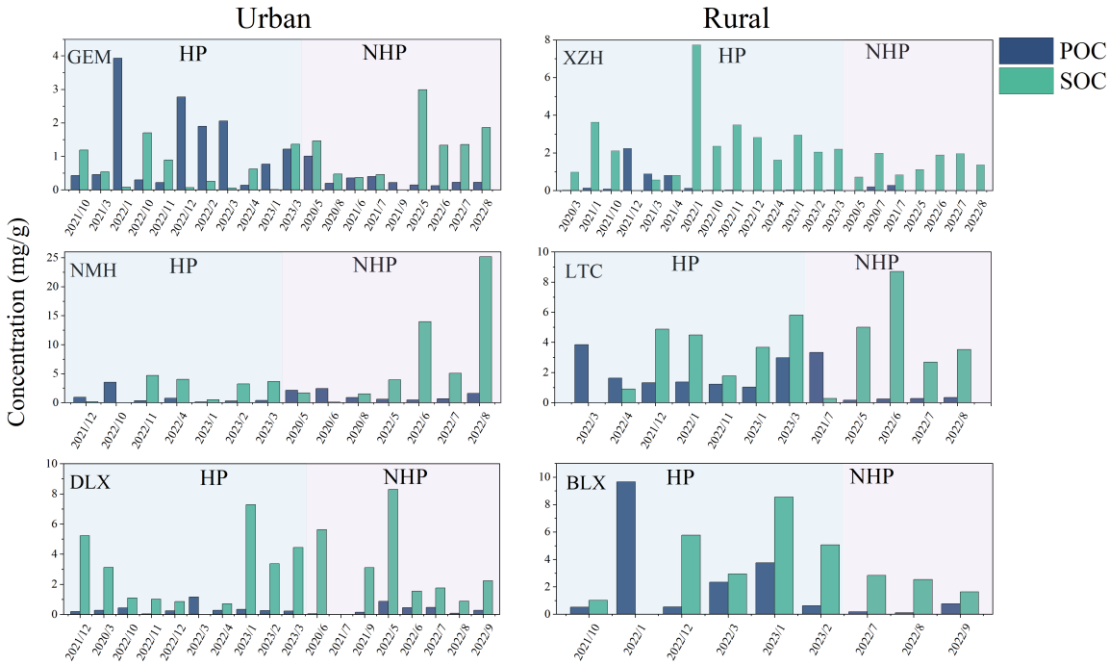

Figure S12 Temporal variations in primary (POC) and secondary organic carbon (SOC) concentration at six monitoring sites during heating and non-heating periods. HP, Heating period; NHP, Non-heating period; XZH, Xiao Zaohuo station; GEM, Golmud station; LTC, Da Gele station; NMH, Nuo Muhong station; BLX, Balong station; DLX, Dulan station.

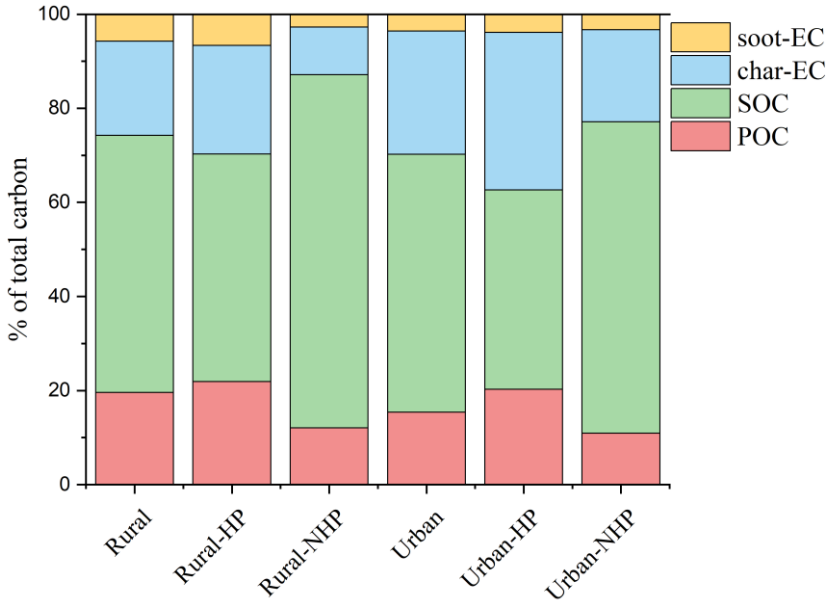

Figure S13 Proportions of various carbon indicators in urban and rural during heating and non-heating periods. HP, Heating period; NHP, Non-heating period.

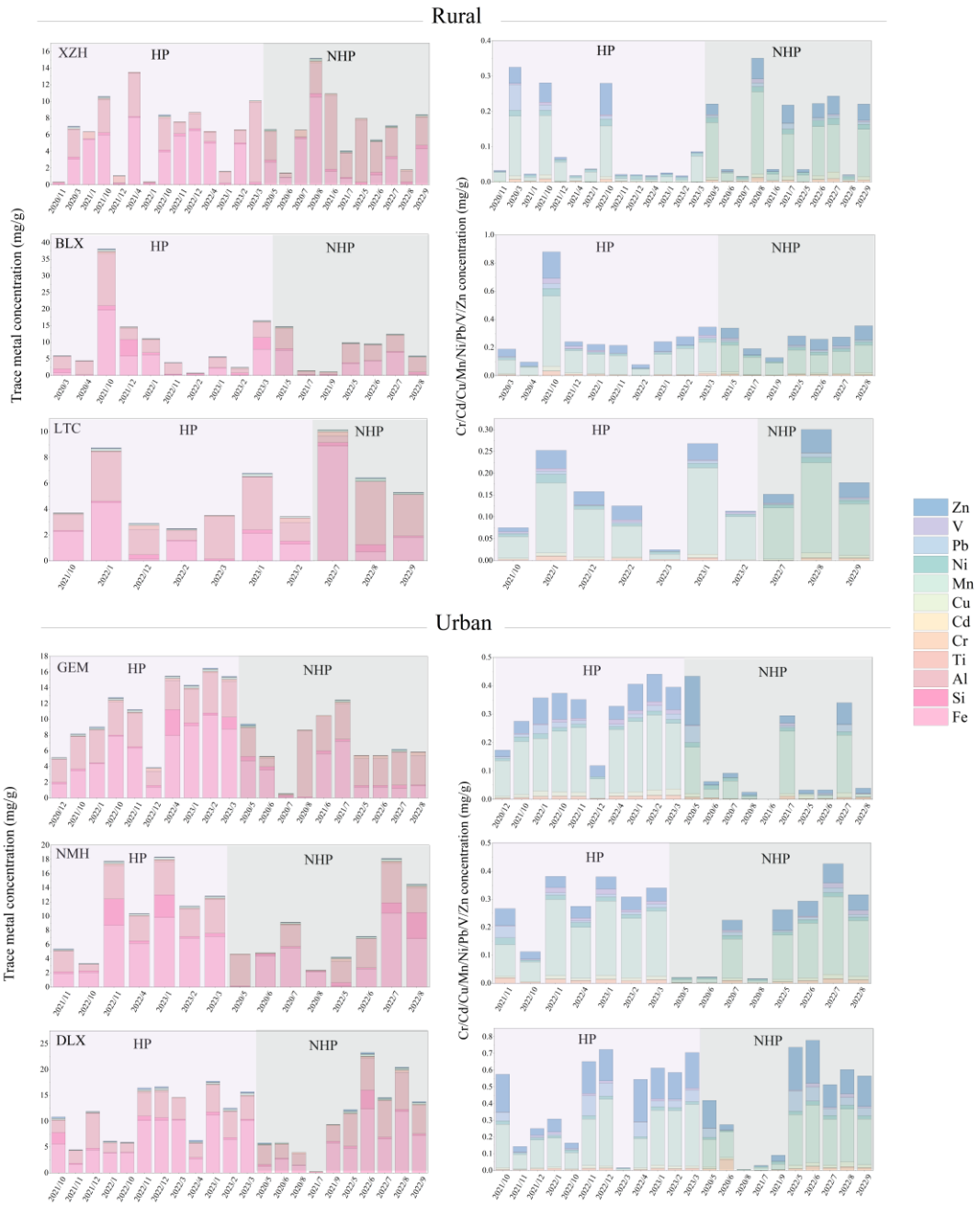

Figure S14 Temporal variations in trace element content at six monitoring sites during heating and non-heating periods. The left panels display trace element concentrations (mg/g) for each site, while the right panels illustrate the smaller concentrations of Cr, Cd, Cu, Mn, Ni, Pb, V, Zn. [HP, Heating period; NHP, Non-heating period; XZH, Xiao Zaohuo station; GEM, Golmud station; LTC, Da Gele station; NMH, Nuo Muhong station; BLX, Balong station; DLX, Dulan station]

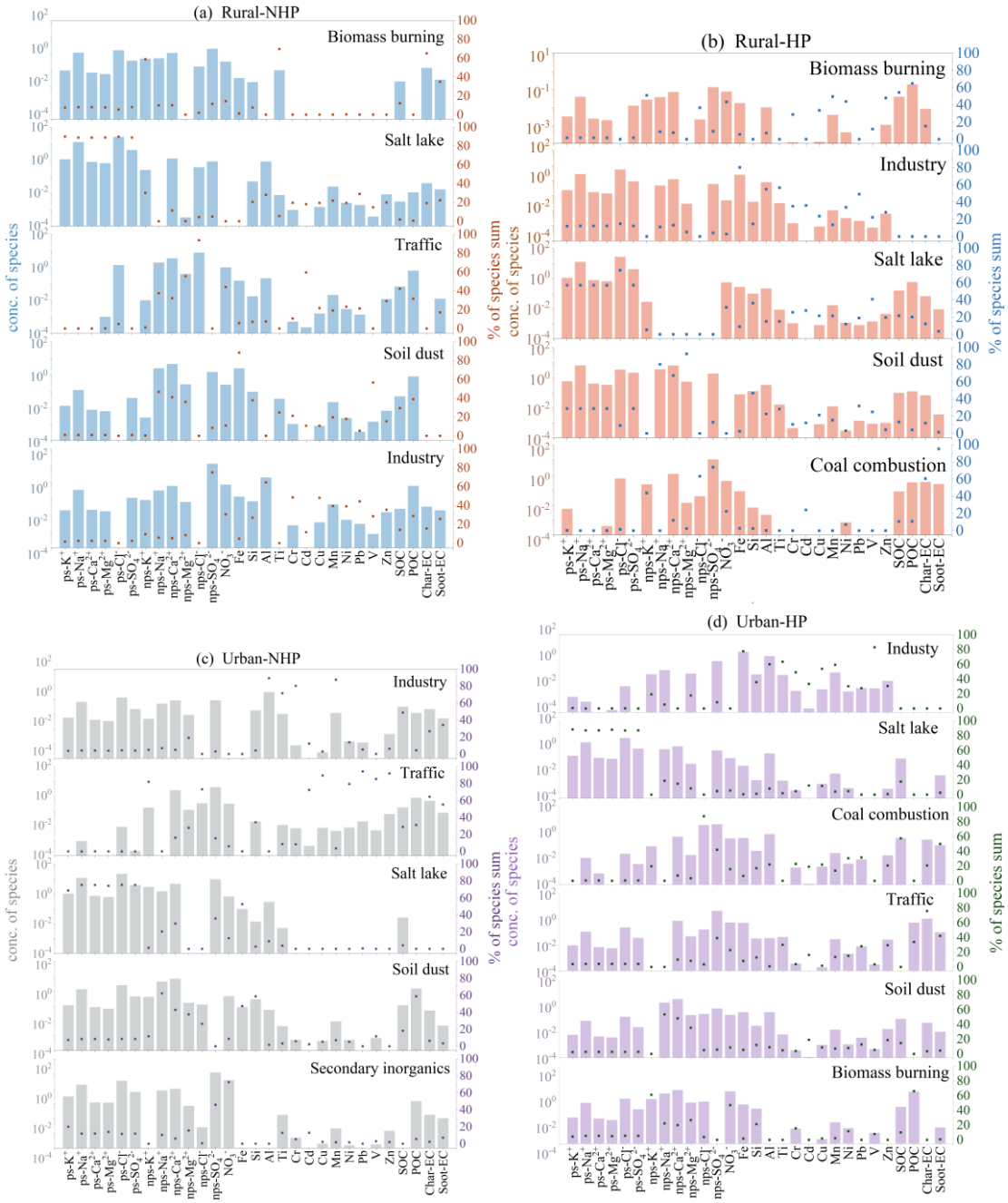

Figure S15 Species profiles and contributions of each resolved source for rural and urban areas during heating and non-heating periods, as determined through PMF dust-fall source apportionment. Contribution of species are presented in a histogram, while the species profile is depicted in a scatter plot. [HP, heating period; NHP non-heating period].

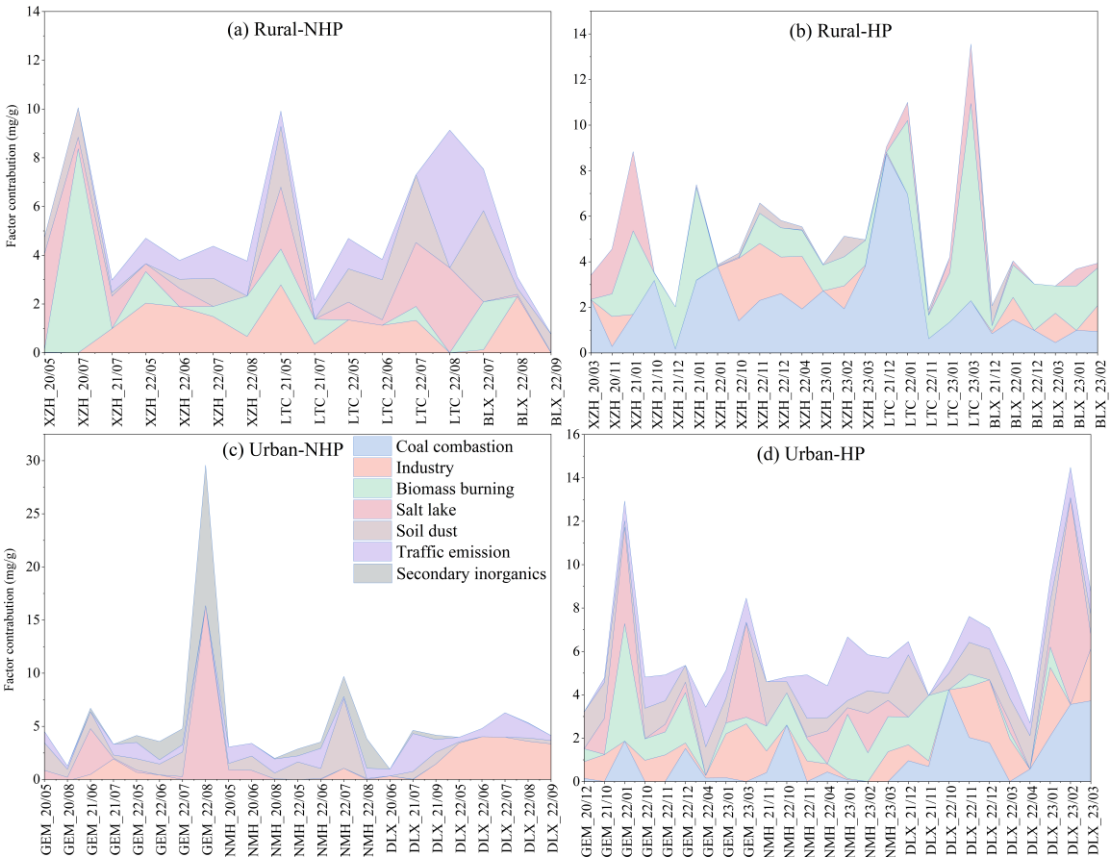

Figure S16 Temporal variations in factor contributions to atmospheric dust deposition in the Qaidam Basin: (a) Rural NHP, (b) Rural HP, (c) Urban NHP, and (d) Urban HP. HP, domestic heating period; NHP, non-domestic heating period.

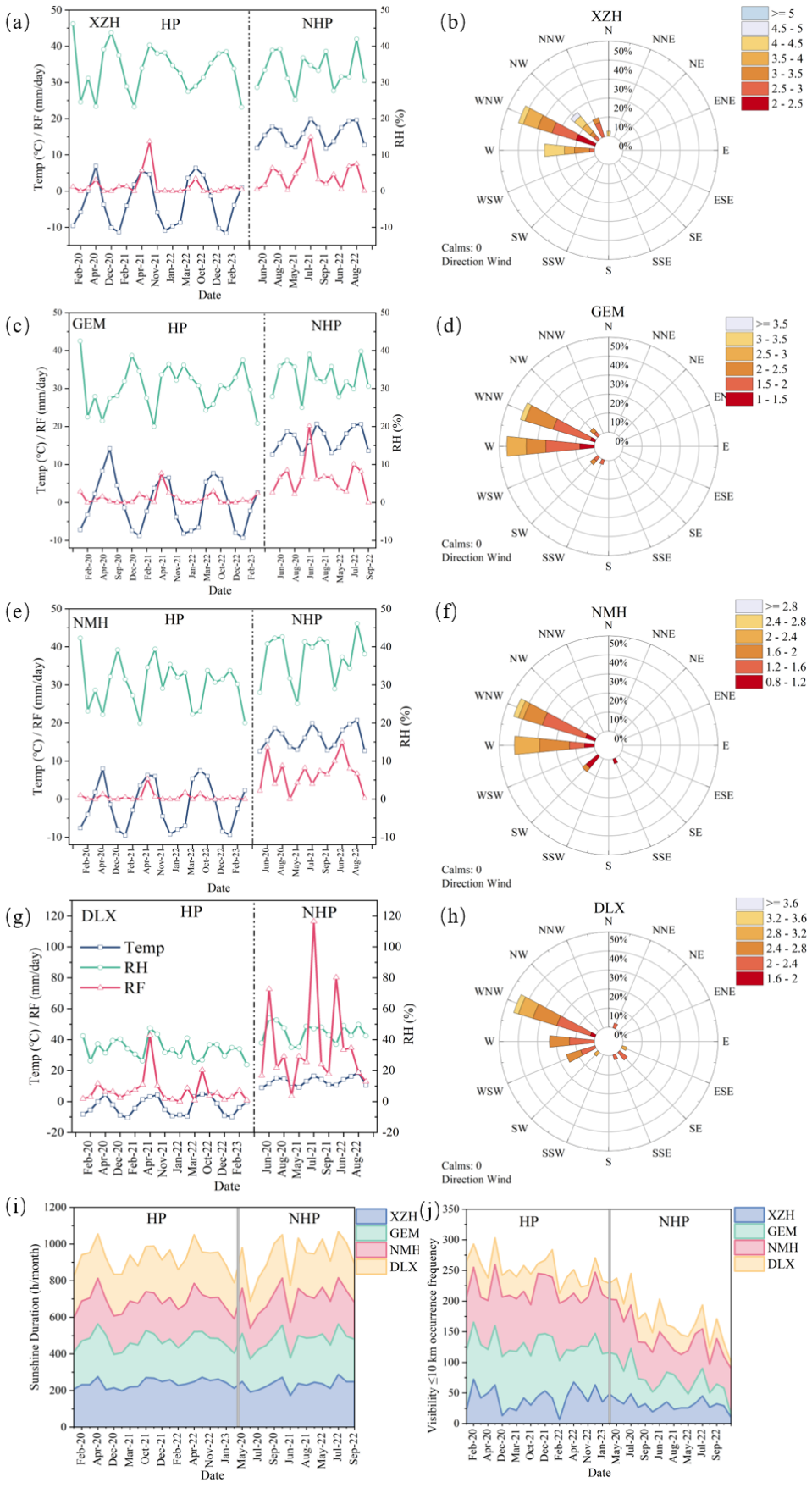

Figure S17 During the sampling period at stations XZH (a, b), GEM (c, d), NMH (e, f), and

DLX (g, h) in the Southern Qaidam Basin: Temperature (Temp), Relative Humidity (RH), Precipitation (RF), Wind Direction, Wind Speed, and Sunshine Duration (i), Visibility ≤10 km occurrence frequency (j). [HP, Heating period; NHP, Non-heating period; XZH, Xiao Zaohuo station; GEM, Golmud station; LTC, Da Gele station; NMH, Nuo Muhong station; BLX, Balong station; DLX, Dulan station].

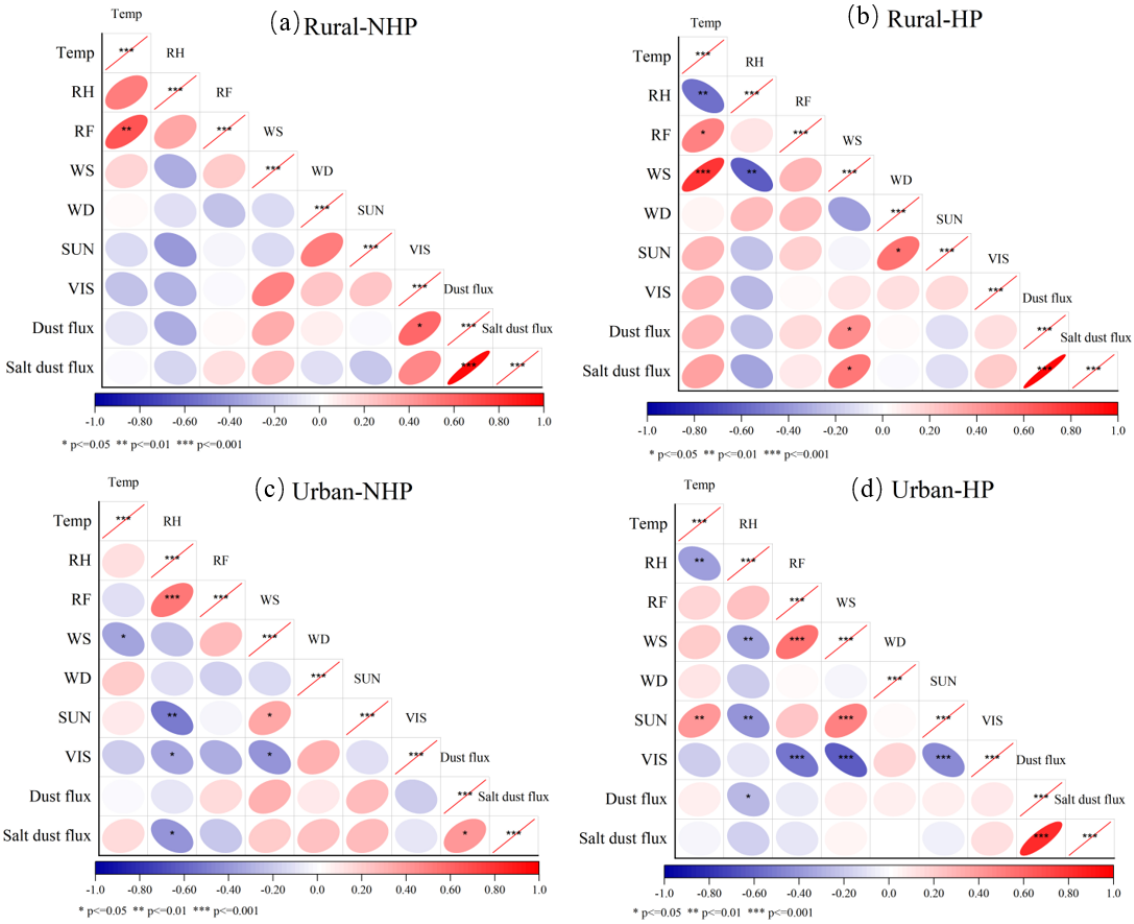

Figure S18 Correlations between meteorological factors and atmospheric dust and salt dust deposition flux in urban and rural areas of the Qaidam Basin during domestic heating (HP) and non-heating (NHP) periods.

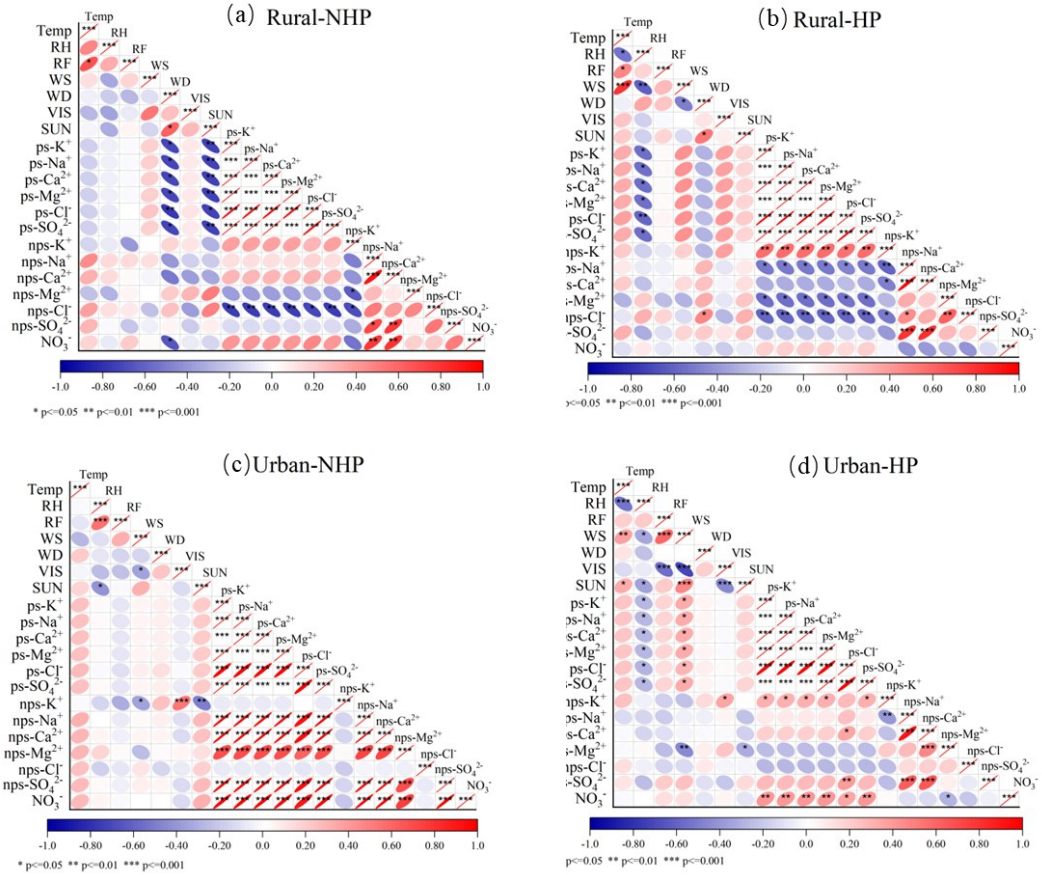

Figure S19 Correlations between meteorological factors and atmospheric dust deposition water soluble ions in urban and rural areas of the Qaidam Basin during domestic heating (HP) and non-heating (NHP) periods.

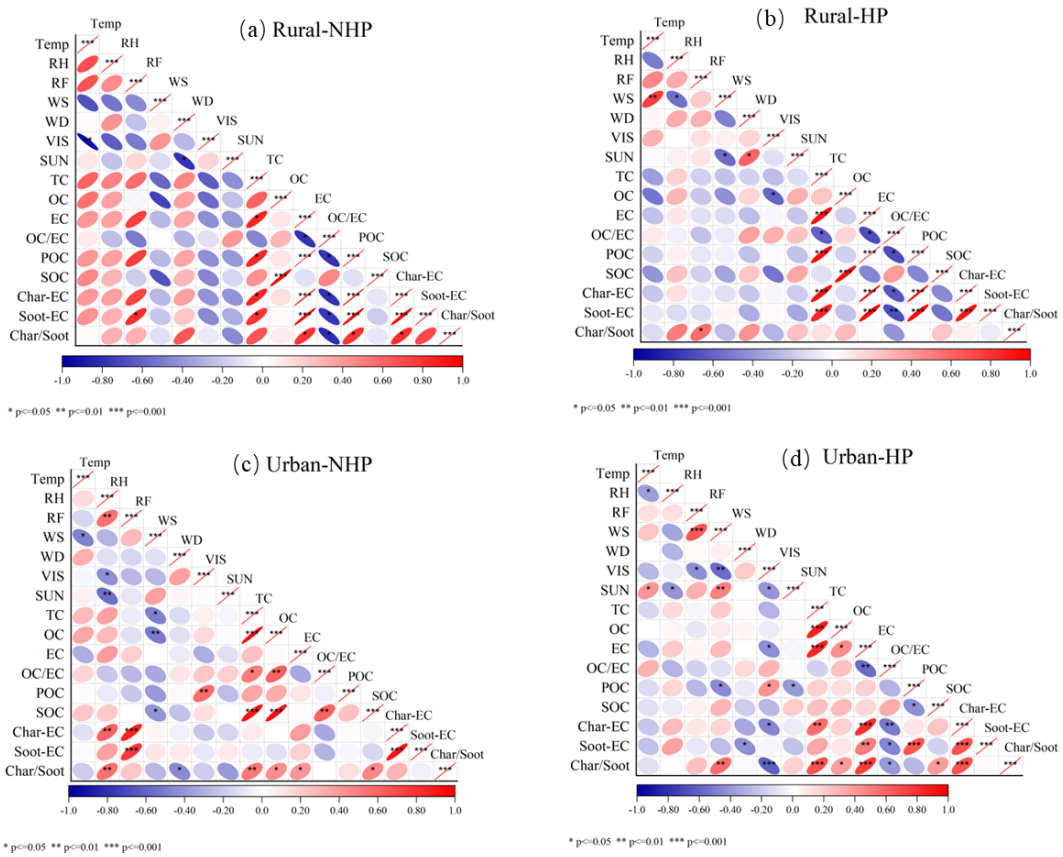

Figure S20 Correlations between meteorological factors and atmospheric dust deposition carbonaceous elements in urban and rural areas of the Qaidam Basin during domestic heating (HP) and non-heating (NHP) periods.

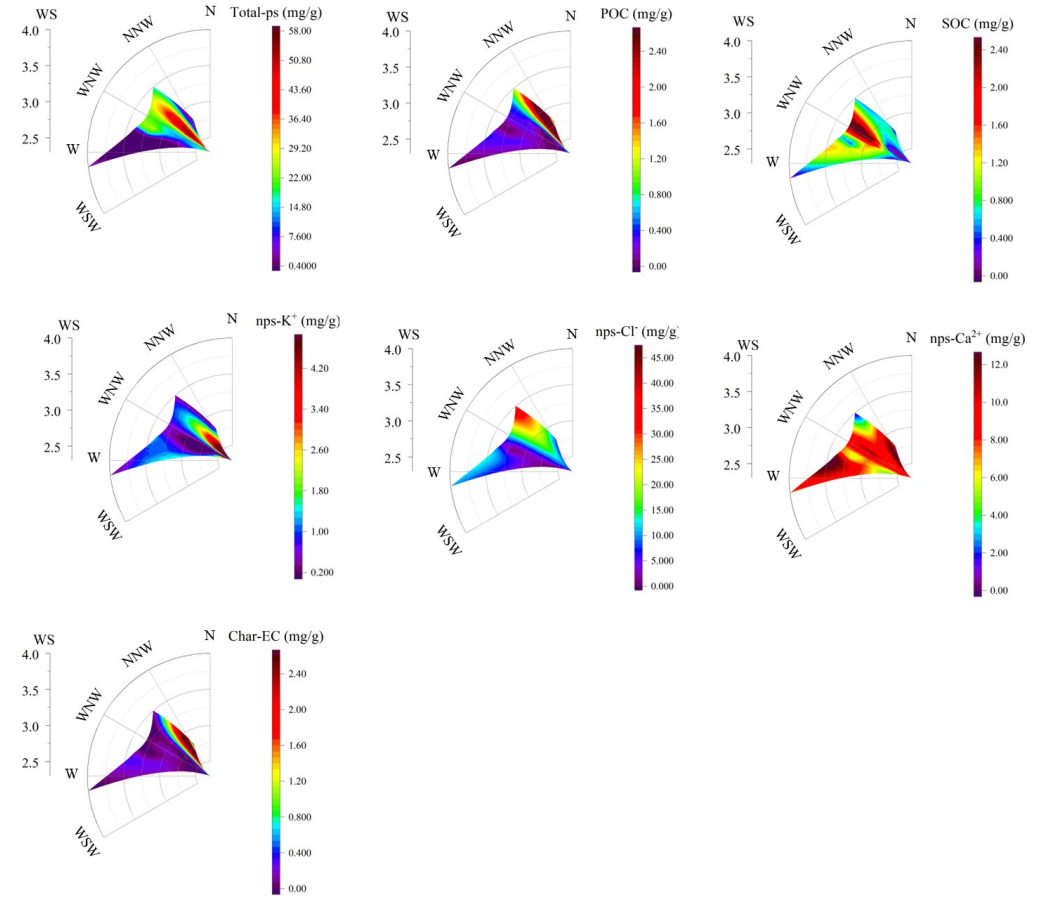

Figure S21 Relationships between wind speed, wind direction, and chemical composition of atmospheric dust deposition in rural of the Qaidam Basin during the domestic heating period (HP).

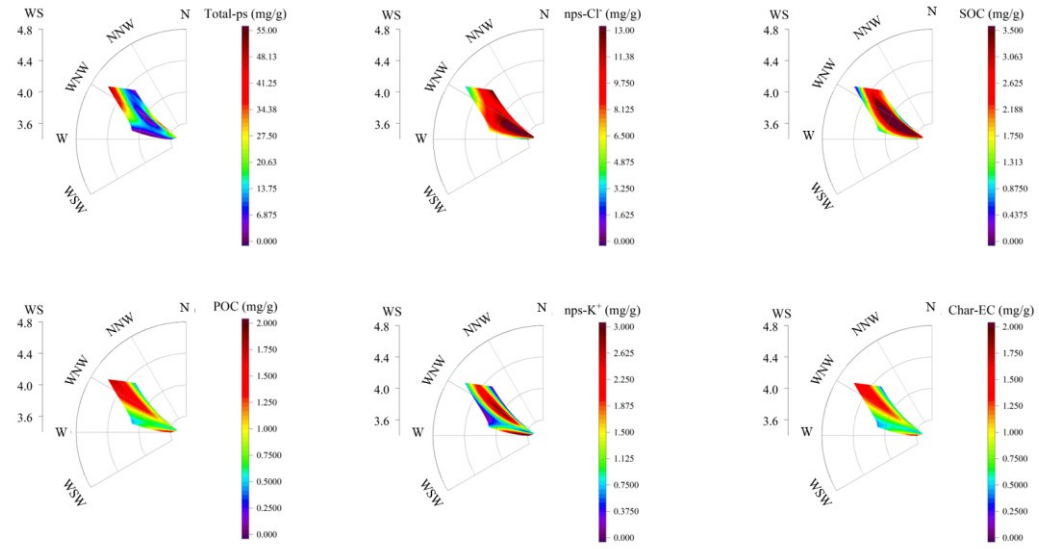

Figure S22 Relationships between wind speed, wind direction, and chemical composition of atmospheric dust deposition in rural of the Qaidam Basin during the non-heating period (NHP).

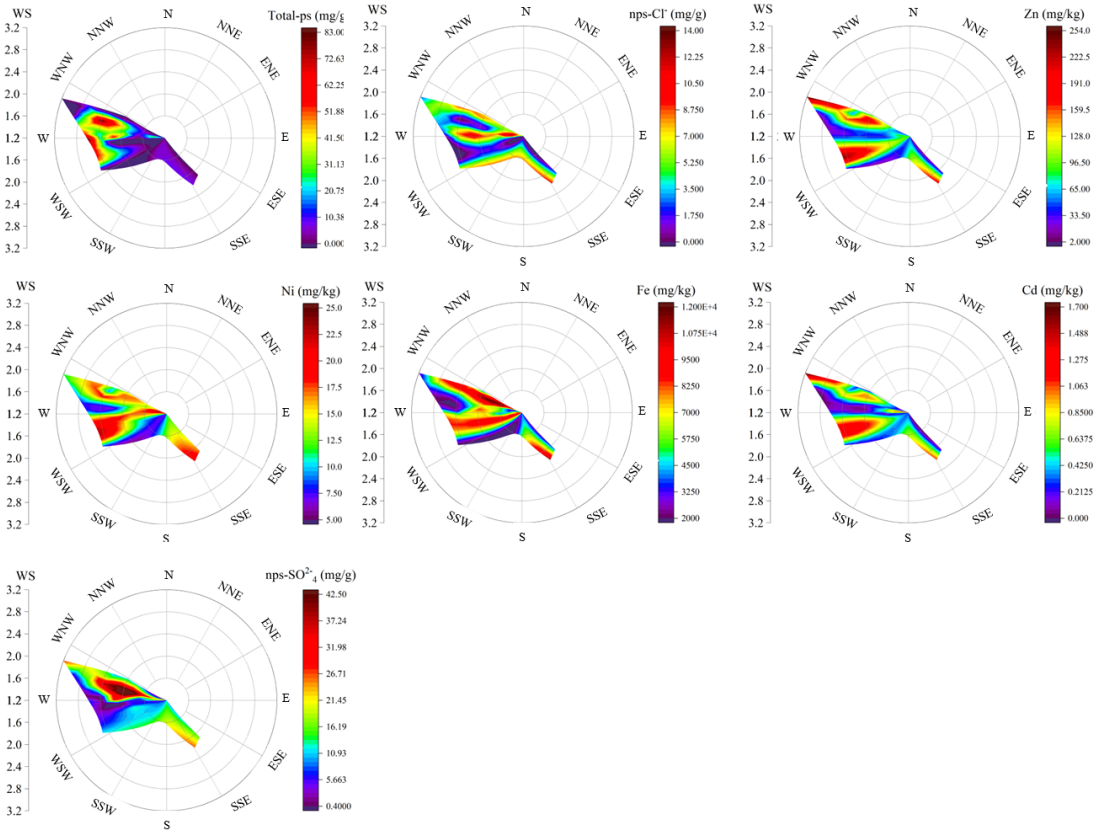

Figure S23 Relationships between wind speed, wind direction, and chemical composition of atmospheric dust deposition in urban of the Qaidam Basin during the domestic he

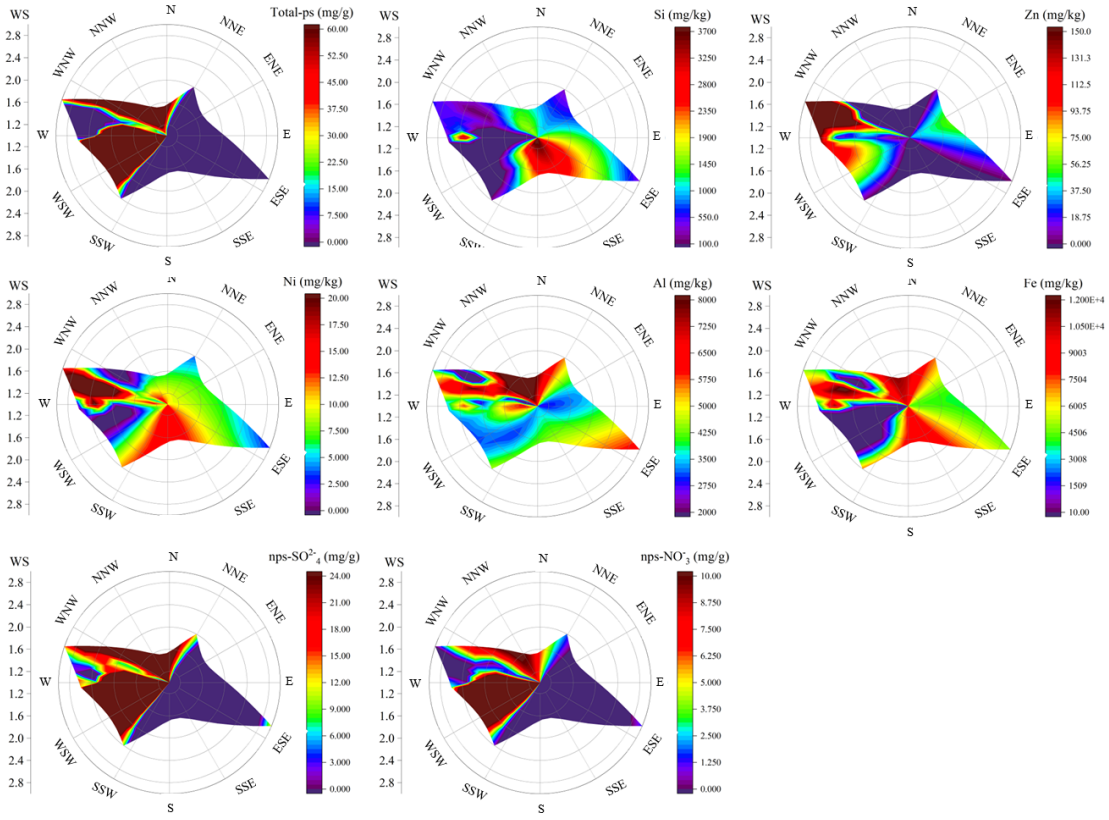

Figure S24 Relationships between wind speed, wind direction, and chemical composition of atmospheric dust deposition in urban of the Qaidam Basin during the non-heating period (NHP).

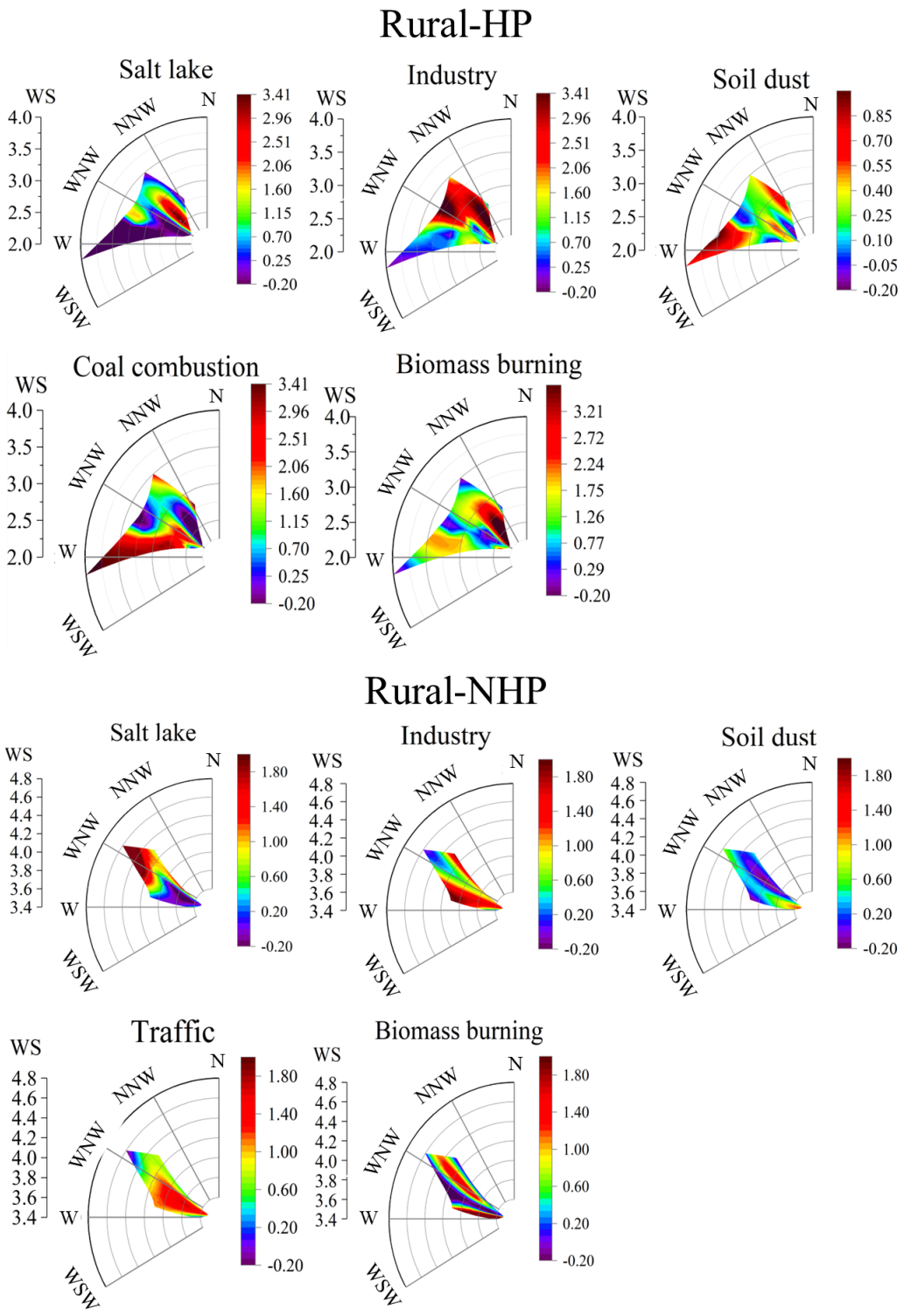

Figure S25 Relationship between wind speed, wind direction, and atmospheric dust deposition sources in rural of the Qaidam Basin during domestic heating (HP) and non-heating (NHP) periods.

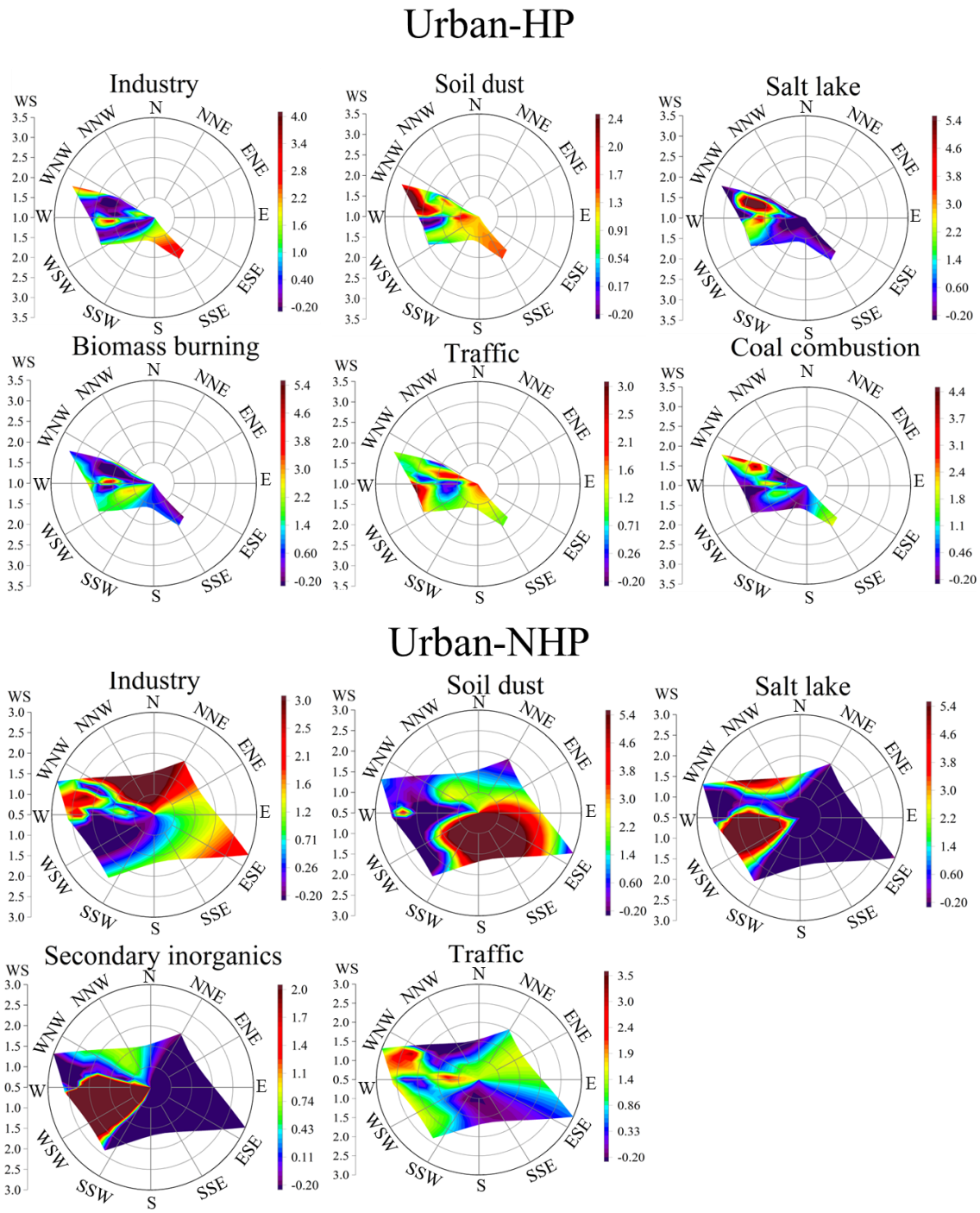

Figure S26 Relationship between wind speed, wind direction, and atmospheric dust deposition sources in urban of the Qaidam Basin during domestic heating (HP) and non-heating (NHP) periods.